

www.acsanm.org Article

Lamellar and Hexagonal Assemblies of PEG-Grafted Silver Nanoparticles: Implications for Plasmonics and Photonics

Hyeong Jin Kim, Wenjie Wang, Wei Bu, Surya K. Mallapragada,* and David Vaknin*



Cite This: ACS Appl. Nano Mater. 2022, 5, 17556-17564



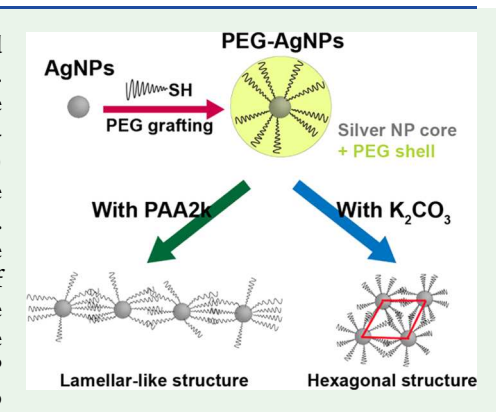
ACCESS

III Metrics & More

Article Recommendations

Supporting Information

ABSTRACT: Assembly of silver nanoparticles (AgNPs) grafted with thiolated poly(ethylene glycol) (PEG-SH) with various molecular weights is reported. Synchrotron-based X-ray surface-sensitive diffraction methods are used to determine the nature of two-dimensional (2D) assemblies at liquid/vapor interfaces, and smallangle X-ray scattering (SAXS) is used to monitor the three-dimensional (3D) assemblies in bulk suspensions. We find that assembly can be induced either by the addition of K_2CO_3 or polyacrylic acid (PAA) to the PEG-AgNP aqueous suspensions. The addition of K_2CO_3 induces a 2D hexagonal structure at the liquid/vapor interface and a 3D hexagonal columnar structure in solutions, where the columns consist of tethered PEG-AgNP chains. On the other hand, the addition of PAA leads to the formation of a 2D lamella-like distorted hexagonal sheet at the liquid/vapor interface and a 3D lamellar superstructure formed by stacked 2D sheets in the PEG-AgNP suspension. Effects of the core type of nanoparticles on the assembly can be used to control structures for potential applications in plasmonics and photonics.



KEYWORDS: silver nanoparticles, nanoparticle assembly, lamellar structures, PEG-grafted silver nanoparticle, X-ray reflectivity (XR), grazing-incidence small-angle X-ray scattering (GISAXS), small-angle X-ray scattering (SAXS)

INTRODUCTION

Major developments in nanotechnology emerged with the demonstration of grafting oxides or noble metals with silane-

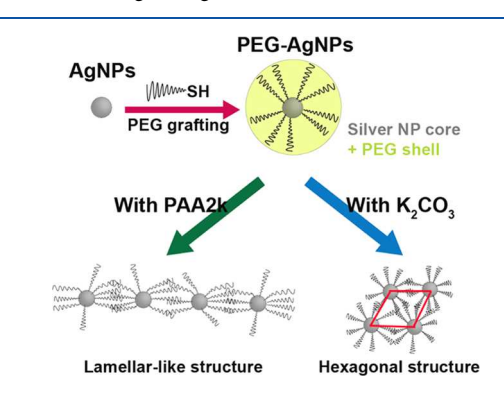


Figure 1. Conceptual illustration of PEG-grafted AgNPs that are water-soluble and manipulated for assembly by adding either K_2CO_3 or PAA to the suspensions. Our results indicate that the addition of K_2CO_3 to PEG-AgNP suspensions induces a hexagonal structure, whereas the addition of PAA induces the formation of chain structures that eventually pack into lamella-like structures.

or thiol-modified polymers, biopolymers, or lipids.¹⁻⁷ Such grafting of nanoparticles allows for the modification of their surfaces such that assembly can be induced and controlled. A challenge in the assembly of nanoparticles is to identify reactive

groups that can be attached to polymers, lipids, or DNA so that they can be grafted to specific nanoparticles (e.g., Si, quantum dot, and Au nanoparticles).^{8–14} Indeed, thiolating single strands of DNA has revolutionized the assembly of nanoparticles, producing a plethora of superstructures in a controlled manner, albeit mostly limited to gold nanoparticles. 15-17 A similar strategy has been employed for grafting nanoparticles with soluble polymers such as poly-(ethylene glycol) (PEG), poly(N-isopropylacrylamide) (PNI-PAM), polyacrylic acid (PAA), polystyrene (PS), and many others. The assembly using this approach is robust and yields relatively simple superstructures, i.e., 1D chain structures, 2D hexagonal structures, and 3D clusters or even fcc-like structures in bulk suspensions, resulting mainly from the intricate balance of the ligand steric repulsion, van der Waals attraction, and hydrogen bonding. 18-31 Most of these studies have been conducted using gold nanoparticles (AuNPs). Here, we extend the studies on the use of PEG as a surface modifier to the assembly of silver nanoparticles (AgNPs) and compare the results with AuNPs. Indeed, the use of Au versus Ag cores is

Received: July 12, 2022 Accepted: November 9, 2022 Published: November 29, 2022





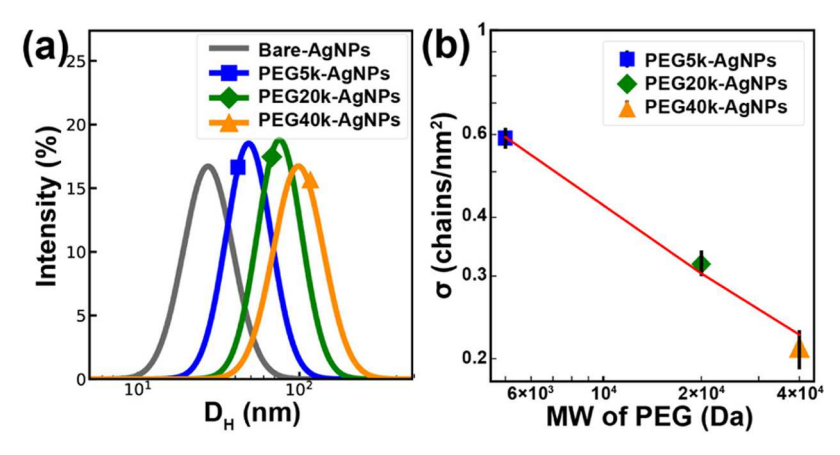


Figure 2. (a) DLS intensity-weighted distribution profiles of the hydrodynamic diameter ($D_{\rm H}$) for bare-surface AgNPs (citrate-stabilized) and PEG-grafted AgNPs with various PEG molecular weights as indicated. (b) Grafting density (σ) of PEG-AgNPs as a function of PEG molecular weights determined by TGA.

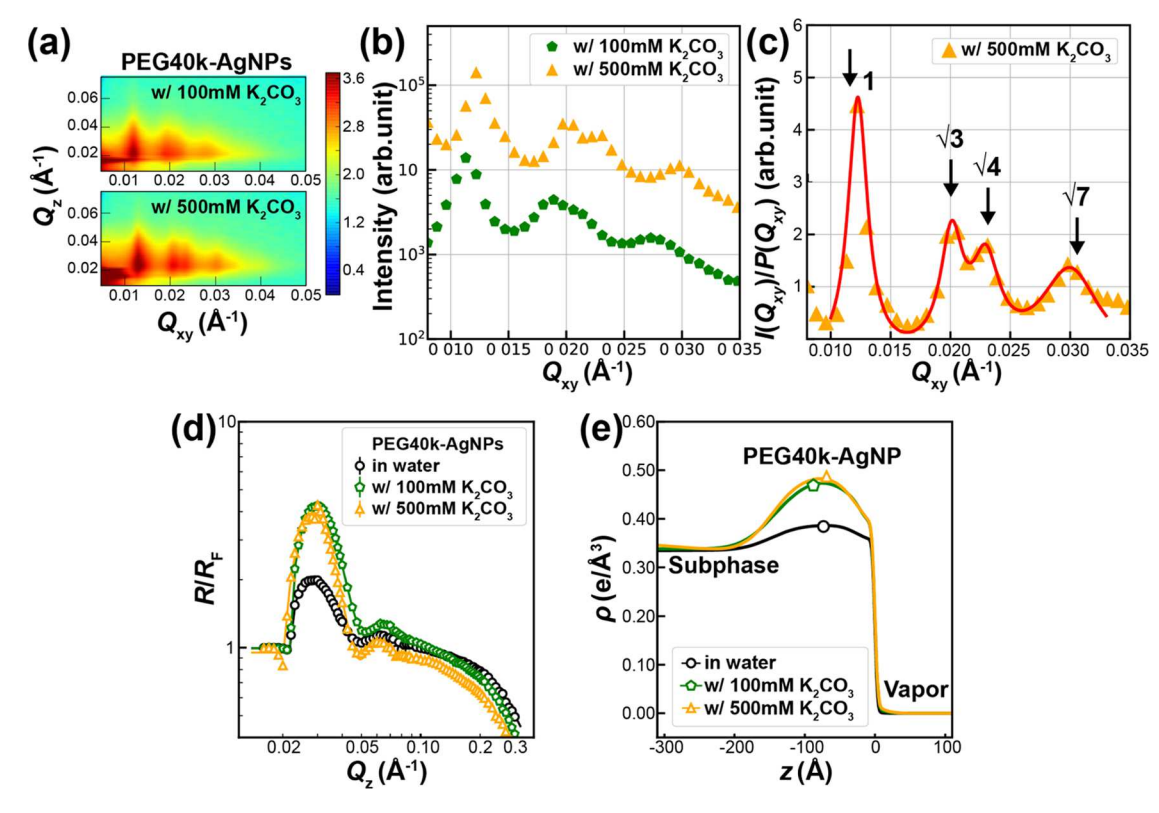


Figure 3. (a) 2D GISAXS images of PEG40k-AgNPs with 100 and 500 mM K_2CO_3 aqueous solutions. (b) In-plane diffraction patterns obtained by horizontal line-cut intensity profiles from GISAXS images in (a). Profiles are shifted vertically for clarity. (c) Extracted structure factor profile $(I(Q_{xy})/P(Q_{xy}))$ for PEG40k-AgNPs with 500 mM K_2CO_3 . The red solid line represents the best-fit profile using Lorentzian-type line shapes, and black arrows indicate the Q positions of higher-order Bragg diffraction peaks of an ideal hexagonal lattice. (d) Normalized reflectivity, R/R_F , data for PEG40k-AgNPs with 0, 100, and 500 mM K_2CO_3 aqueous solutions. (e) Electron density (ED) profiles obtained from the best-fit to the R/R_F data shown in (d). The bell shape of ED is dominated by the core AgNPs, indicating surface density saturation at 100 mM K_2CO_3 .

particularly interesting as they highlight a potential handle for leveraging the core type to control PEG-mediated assembly. Such assembled systems are sought for applications in plasmonics or photonics. There is evidence that the thiol group interacts with gold and silver differently. $^{32-36}$ Indeed, theoretical models show that the metal—thiol bond is partially electrostatic and covalent and that the covalent bond decreases in the order of Au > Cu > Ag. 32 Our approach toward grafting and assembling silver nanoparticles is illustrated in Figure 1. We note that the assembly of PEG-grafted AgNPs (PEG-

AgNPs) is induced by manipulating the salinity of the suspensions, adding PAA, and/or varying their temperature.

EXPERIMENTAL SECTION

Material Preparation. Citrate-stabilized silver nanoparticles (AgNPs) of ~20 nm diameter were purchased from NanoComposix Inc. Their size and dispersity are further verified by small-angle X-ray scattering technique (see Figure S2). AgNPs are grafted with poly(ethylene glycol) (PEG) by a ligand-exchange protocol from citrate to thiolated PEG (PEG-SH; purchased from Creative PEGWorks). Briefly, citrate-stabilized AgNPs in aqueous solutions

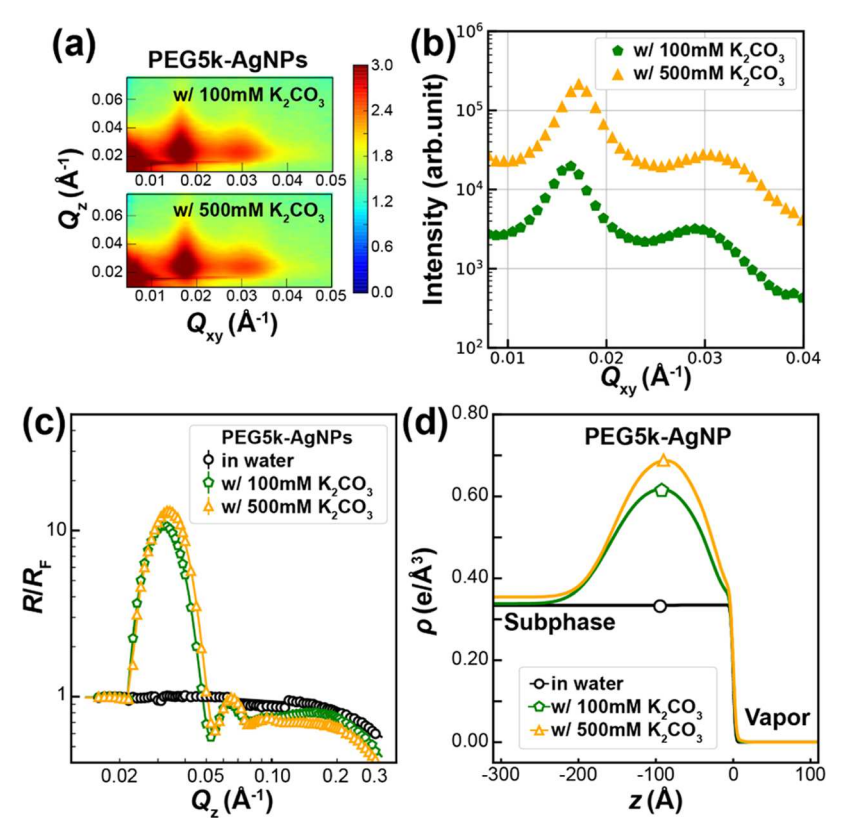


Figure 4. (a) 2D GISAXS images of PEG5k-AgNPs with 100 and 500 mM K_2CO_3 aqueous solutions. (b) Horizontal line-cut intensity profiles from GISAXS images in (a). Profiles are shifted vertically for clarity. (c) R/R_F data of PEG5k-AgNPs with 0, 100, and 500 mM K_2CO_3 aqueous solutions. Note: the discontinuity in the R/R_F (black circles) is due to some random cause such as surface inhomogeneity when PEG-AgNPs sporadically populate the surface in the absence of salts. (d) One of the best-fit ED profiles corresponding to the R/R_F data shown in (c).

Table 1. Summary of GISAXS and XR Results for PEG-AgNPs under Various Solvent Conditions

nanoparticle type	solvent condition	lattice type	d -spacing $(nm)^a$	$\Gamma_{\rm e}({\rm e}/{\rm \AA}^2)^b$
PEG40k-AgNPs	in pure water	lamella-like	94 (3)	~6.7
	with 0.2 mM PAA2k	lamella-like	76 (4)	~10.3
	with 2 mM PAA2k	lamella-like	61 (3)	~17.2
	with 100 mM K ₂ CO ₃	2D hexagonal	57 (1)	~18.2
	with 500 mM K ₂ CO ₃	2D hexagonal	54 (2)	~19.3
PEG20k-AgNPs	in pure water	lamella-like	60 (3)	~6.1
	with 2 mM PAA2k	lamella-like	54 (3)	~23.6
	with 100 mM K ₂ CO ₃	2D hexagonal	48 (1)	~14.7
	with 500 mM K ₂ CO ₃	2D hexagonal	47 (2)	~26.7
PEG5k-AgNPs	in pure water	n/a (background-like)		
	with 2 mM PAA2k	n/a (form factor-like)		~9.2
	with 100 mM K ₂ CO ₃	2D hexagonal	38 (1)	~35.1
	with 500 mM K ₂ CO ₃	2D hexagonal	36 (2)	~40.5

^aInterparticle distance from the best-fit profile using Lorentzian-type line shapes; $d = 2\pi/Q_{10}$ for the (10) peak. ^bExcess surface electron density in ED profiles, $\Gamma_{\rm e} = \int [\rho(z) - \rho_{\rm sub}(z)] {\rm d}z$.

are incubated with PEG-SH for about 4 h at a concentration of ~4 molecules of PEG-SH per nm² of AgNP surface area. The Assuming that the cross-section of PEG-SH is of the order of 0.3 nm², the concentration of PEG-SH is approximately 1.3 times that required for the complete coverage of each AgNP. Subsequently, grafted AgNPs are separated from the suspension by repeated centrifugation at 10 000g three times each for 1 h. To characterize the grafting of AgNPs, we use UV—vis absorption methods, dynamic light scattering (DLS), and thermogravimetric analysis (TGA), as described elsewhere. The Agnetic Period of the suspension of the processing software Zetasizer (Malvern, U.K.). DLS data were processed into intensity percentage versus hydrodynamic size distribution profiles. In this study, we use these size distribution

profiles as a qualitative means to verify the success of grafting as nanoparticles grafted with a longer PEG manifest a larger hydrodynamic size on average. ^{27,30} Figure 2a shows the distribution of the hydrodynamic diameter of as-purchased and grafted AgNPs with different PEG molecular weights. It shows that the intensity distribution profile shifts to a larger hydrodynamic size on average with higher PEG molecular weight as expected from grafted nanoparticles, i.e., the longer the ligand chain, the thicker the PEG corona. More quantitative measurements of the PEG grafting density were performed with a TGA Netzsch STA449 F1. For TGA measurements, dried PEG-grafted AgNPs were prepared on alumina crucibles and gradually heated up to 625 °C under a nitrogen atmosphere. The mass change of AgNP samples was measured over

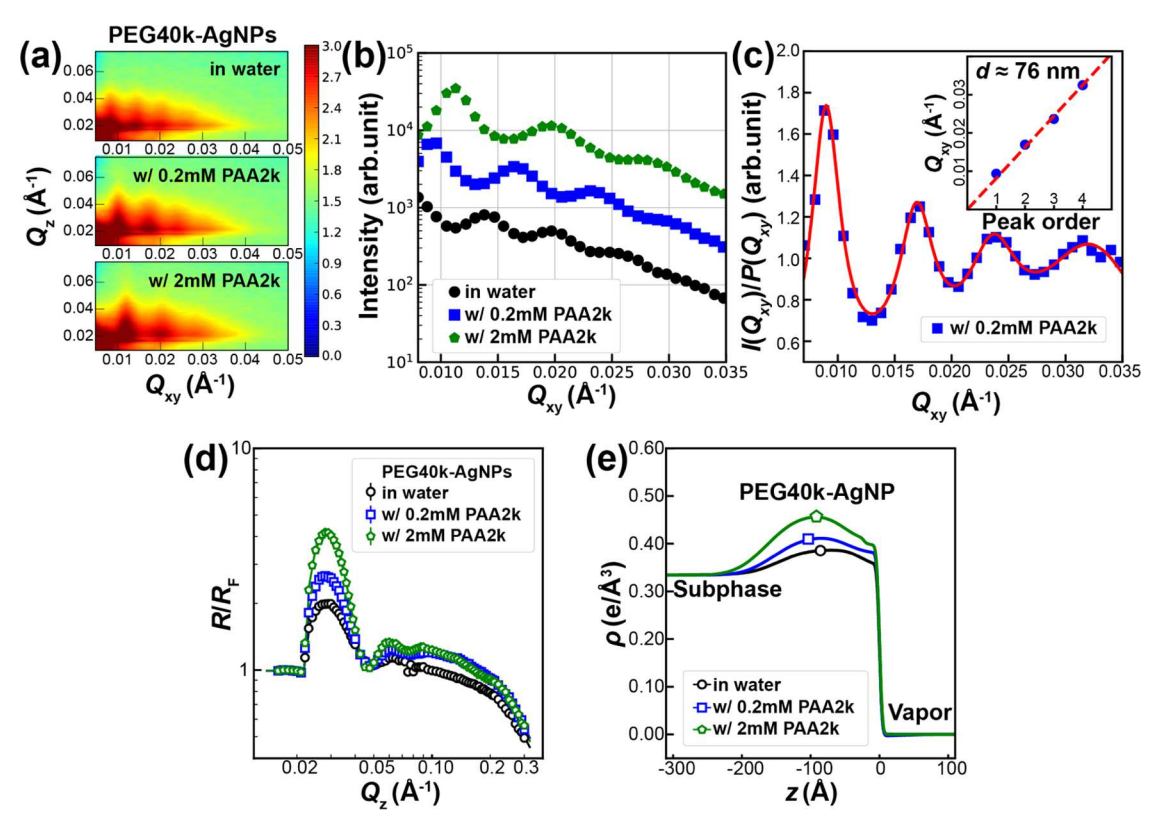


Figure 5. (a) 2D GISAXS images of PEG40k-AgNPs with 0, 0.2, and 2 mM PAA2k aqueous solutions. (b) Horizontal line-cut intensity profiles from GISAXS images in (a). Profiles are shifted vertically for clarity. (c) Extracted structure factor profile $(I(Q_{xy})/P(Q_{xy}))$ for PEG40k-AgNPs with 0.2 mM PAA2k. The red solid line is the best-fit profile using Lorentzian-type line shapes. Inset: peak position, Q_{xy} , as a function of the peak order with a linear fit with a slope estimation of interparticle distance, d. (d) R/R_F data for PEG40k-AgNPs with 0, 0.2, and 2 mM PAA2k aqueous solutions. (e) One of the best-fit ED profiles corresponding to the R/R_F data shown in (d).

the heating process. As a result of the thermal degradation of PEG around 300-450 °C, the mass loss of AgNP samples was used to determine the PEG grafting density. Figure 2b shows the grafting density of PEG-AgNPs as a function of the PEG molecular weight. This is consistent with former studies that showed that the grafting density of AgNPs is not as high as that of gold nanoparticles. The final concentration of PEG-AgNPs is determined by UV-vis absorption methods, calibrated and standardized with vendorprovided information (Molecular Devices, SpectraMax M3).24 PEG molecules of molecular weight (MW) 5, 20, and 40 kDa are grafted onto the AgNP surface as ligands. PEGxk-AgNP denotes the silver nanoparticle grafted with PEG with MW x kDa. Based on earlier reported studies, it is expected that the larger the MW of the ligand PEG, the lower the threshold (e.g., salt concentration and solution temperature) to induce the assembly of PEG-grafted nanoparticles. 20,23

X-ray Experimental Setup. In this study, we use surface-sensitive X-ray diffraction methods to determine the structures of the films at the liquid/vapor interface in situ. Small-angle X-ray scattering (SAXS) is used to investigate the 3D structures of the assembly in bulk suspensions. These methods employ synchrotron-based X-ray scattering, which was conducted at the Advanced Photon Source, Argonne National Laboratory. For the liquid surface-sensitive 2D Xray diffraction, X-ray reflectivity (XR) and grazing-incidence smallangle X-ray scattering (GISAXS) were conducted on beamline 15 ID-C, NSF's ChemMatCARS, with a liquid surface spectrometer (X-ray energy, E = 10 keV). For the 3D assembly, SAXS measurements were carried out at beamline 12 ID-B with X-ray energy, E = 13.3 keV. Both beamlines use area detectors to record scattering intensities as a function of Q, the scattering vector. At 15ID-C, a Pilatus 200K is placed 1040 mm away from the sample center to collect XR and GISAXS signals. For SAXS at 12ID-B, a Pilatus 2M is used at a distance of 2010 mm from the sample. The intensities are further

reduced into intensity profiles on-site with beamline correction protocols accordingly. Below is a brief description of the methodologies. For the liquid surface X-ray scattering measurements (XR and GISAXS), the sample solution is placed in a shallow trough of 1.5 mL volume and approximately 2 × 10 cm² surface area. A highly collimated and monochromatic X-ray beam is incident on the surface at an angle of α_i with respect to the air/water interface. For XR, the exit angle, α_f , of the reflected beam is maintained at $\alpha_f = \alpha_i$ for a series of α_i 's. The reflectivity, R, is recorded as a function of Q_z , where Q_z is the vertical component of the scattering vector, and $\mathbf{Q}_z=\frac{4\pi}{\lambda}\sin\,\alpha_{\rm i}$ (λ being the X-ray wavelength). Here, we display the normalized reflectivity $R/R_{\rm F}$, where $R_{\rm F}$ is calculated for an ideal solution/air interface. The $R/R_{\rm F}$ is fitted to an electron density (ED) profile, $\rho(z)$, across the interface as a function of depth z in the vertical direction using the Parratt recursive method. $^{40-42}$ The GISAXS intensity data are recorded as a function of Q_z and Q_{xyy} where Q_{xy} is the horizontal component of the scattering vector. 40,42 It is performed at incident beam angle $\alpha_i = 0.0906^\circ$, approximately $0.74\alpha_c$, where α_c is the critical incident angle for total reflection for an air/solution interface and is ≈0.1227° for pure water in this study. The line-cut intensity profile along Q_{xy} that is integrated over $Q_z = 0.018-0.05 \text{ Å}^{-1}$, typically featuring Bragg-reflection-like peaks, is used to extract the in-plane ordered arrangement of the particles.

SAXS is aimed at unraveling the structure of the assembly in the suspensions that are contained in capillaries normal to the incident X-ray beam. The intensity is recorded as a function of Q, the magnitude of the scattering vector. The SAXS intensity profiles for PEG-AgNP suspensions are denoted as I(Q). The structure factor of the assemblies, S(Q), is proportional to I(Q)/P(Q). The intensity from well-dispersed AgNPs that are stabilized in citrate solution (see scaled P(Q) in Figure S2). P(Q) is proportional to I(Q)/P(Q), where I(Q) is the form factor amplitude of a solid sphere of

known diameter. Additional details on the experimental setups and analysis of X-ray scattering measurements can be found in previously reported studies. ^{25,26,29}

RESULTS AND DISCUSSION

2D Crystallization. Figure 3a,b displays examples of 2D GISAXS intensity colormaps and corresponding 1D intensity

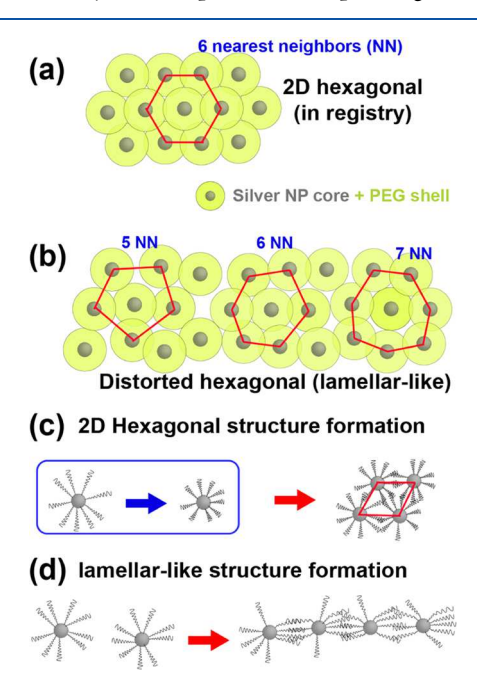


Figure 6. (a and b) Schematic illustration of the 2D hexagonal and distorted hexagonal structures of PEG-AgNPs at the liquid/vapor interface induced by K_2CO_3 or PAA, respectively. The distorted hexagonal structure can be viewed as unregistered chains of AgNPs (registered chains produce a 2D hexagonal structure). Another way to view the distorted hexagonal structure is that the nearest neighbor (NN) of a typical nanoparticle varies between 5 and 7 distribution (in the hexagonal structure, NN is exactly 6). (c and d) Schematic illustrations of the proposed formation mechanism for 2D hexagonal and lamella-like structures of PEG40k-AgNPs at the liquid/vapor interface. Note: these drawn schemes have been exaggerated for visualization purposes.

profiles. Other than the extremely low Q_{xy} and low Q_z regions in the 2D map that are dominated by the reflected beam, the scattering is concentrated near $Q_z \approx 0.019 \text{ Å}^{-1}$ and peaked at a discrete set of Q_{xy} positions. Figure 3a shows GISAXS images for PEG40k-AgNPs with 100 and 500 mM of K_2CO_3 aqueous solutions. Figure 3b shows the horizontal line-cut intensity profiles (integrated over a Q_z range of 0.018–0.05 Å⁻¹) from GISAXS images in (a), displaying diffraction patterns that indicate ordering. The line-cut intensity is normalized to P(Q) (the scattering intensity of a single AgNP), $I(Q_{xy})/P(Q_{xy})$, and is shown in Figure 3c. A fit to the diffraction peaks using Lorentzian-type line shapes reveals that the diffraction peaks are most consistent with a 2D hexagonal structure based on a relative peak position ratio of $\sim 1: \sqrt{3}: \sqrt{4}: \sqrt{7}$ with the lattice constant $a \sim 62$ nm.

X-ray reflectivity (XR) is used to determine the thickness of the ordered film, as shown in Figure 3d for the same sample used in GISAXS measurements. $R/R_{\rm F}$ data show a higher first maximum and stronger oscillations with an increase in the K_2CO_3 concentration from 0 to 100 mM at which saturation is

reached. This shows that PEG40k-AgNPs spontaneously migrate to the liquid/vapor interface and form a Gibbs monolayer. For quantitative analysis, electron density (ED) profiles are obtained from R/R_F data in (a) by following standard analysis in terms of a box-model. 40-42 The enhanced ED profile over the z range from -200 to 0 Å is close to the core size of a silver nanoparticle (the nominal diameter of purchased AgNPs is close to 20 nm), proving the formation of a monolayer. We note that the overall ED profile is dominated by the core silver nanoparticle due to a much higher electron density of silver than the grafted PEG. PEG has an ED very close to that of water and thus cannot be readily distinguished from the surrounding medium in XR measurements. The size distribution of AgNPs in citrate solution has also been determined by SAXS measurements, as shown in Figure S2, yielding an average diameter of 21.0 \pm 2.9 nm. Similar GISAXS and XR observations are made for the shorter PEG chains (i.e., PEG20k and PEG5k), albeit with smaller lattice constants (see Figures 4, S3, S4, and S5). As shown in Figures 4a,b, the diffraction patterns consist of broad peaks implying inferior crystal quality for PEG5k-AgNPs. This is consistent with previous results using PEG-grafted gold nanoparticles (PEG-AuNPs), showing that the PEG chain length affects the conditions under which assembly is induced or crystal quality formation. 24,28,30 XR data and analysis of PEG5k-AgNPs also show the formation of a Gibbs monolayer at the liquid/vapor interface (see Figure 4c,d). Additional data for PEG20k-AgNPs are available in the SI (see Figures S3 and S6).

Using the GISAXS data in combination with XR, the surface coverage of the ordered NPs can be estimated as described in detail previously.²⁴ Our results show that the coverage of PEGAgNPs is of the order of 55–60%, which is smaller than that of PEG-AuNPs for which the coverage is close to 100%. Table 1 lists the extracted parameters for the above-mentioned systems.

Figure 5a,b shows the diffraction patterns for PEG40k-AgNPs in pure water and in PAA solutions. As PAA is added, the Bragg peaks get more intense and sharper, indicating improved crystallinity (see Figure 5a,b). Interestingly, adding PAA to the PEG-AgNP suspensions, instead of K₂CO₃, yields a 2D assembly with a different diffraction pattern. Figure 5c shows that the diffraction pattern consists of equidistant peaks, characteristic of lamella-like structures. The inset in Figure 5c shows that the higher-order peaks are integer multiples of the fundamental peak position of ~1:2:3:4, typically seen in the diffraction patterns from lamellar structures. A more detailed illustration can be seen in the SI (e.g., Figure S5). We argue that such a 2D diffraction pattern can arise from a distorted hexagonal structure that can be viewed in two ways. 44,45 One, where chains of PEG-AgNPs are formed, featuring a longitudinal interparticle correlation; however, unlike the perfect 2D hexagonal structure, the registry between adjacent chains is irregular (no registry in the transverse direction). Another, and similar, view is that the number of nearest neighbors (NN) for a typical nanoparticle varies randomly between 5 and 7 NN, as illustrated in Figure 6a,b (in the hexagonal structure, NN is exactly 6).

 $R/R_{\rm F}$ data and extracted ED profiles for PEG40k-AgNPs show that the increase in PAA in the suspension increases the PEG-AgNPs at the interface (Figure 5d,e). For relatively long PEG chains, such as PEG40k and PEG20k, spontaneous interfacial assembly of PEG-AgNPs is observed, even without any electrolytes added, as shown in Figures 5 and S3. This is likely due to a significant increase in the number of PEG

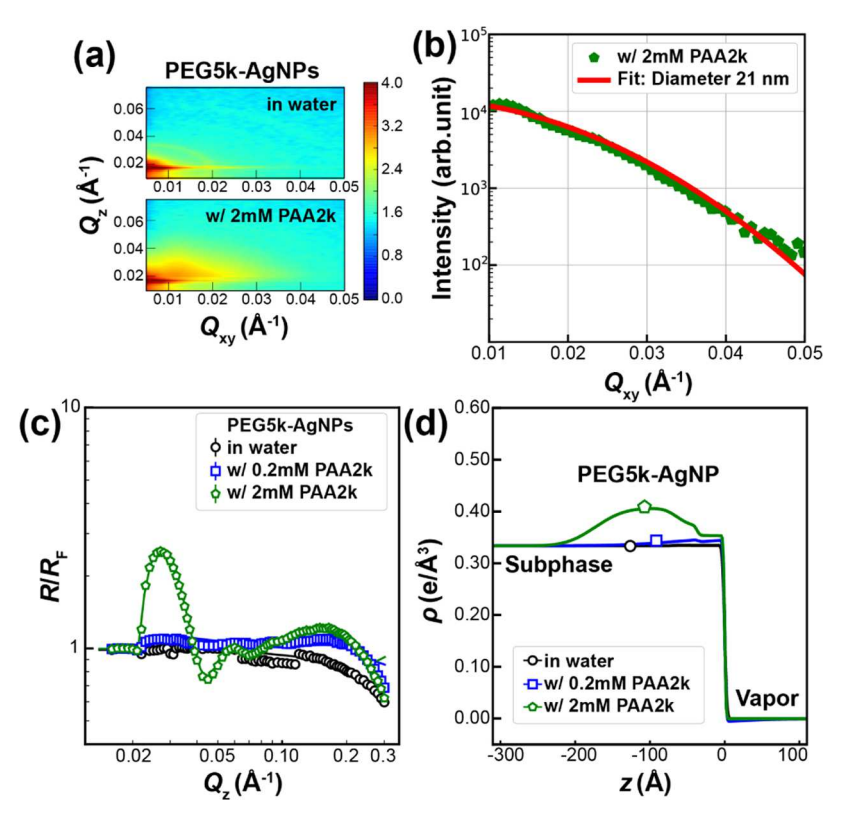


Figure 7. (a) 2D GISAXS images of PEGSk-AgNPs with 0 and 2 mM PAA aqueous solutions. (b) Horizontal line-cut intensity profile from GISAXS images in (a). The red solid line represents the best-fit profile using the form factor of a sphere with \sim 21 nm diameter. (c) $R/R_{\rm F}$ data for PEGSk-AgNPs with 0, 0.2, and 2 mM PAA aqueous solutions. Note: the discontinuity in $R/R_{\rm F}$ (black circles) is due to some random cause such as surface inhomogeneity when PEG-AgNPs sporadically populate the surface in the absence of PAA. (d) One of the best-fit ED profiles corresponding to the $R/R_{\rm F}$ data shown in (c).

monomers per nanoparticle, leading to spontaneous film formation as previously observed in long-chain PEG-grafted AuNPs.²⁷ Such a 2D lamella-like film is presumably the building block that forms the 3D layered structure described in the 3D Crystallization Section, below. Table 1 lists the extracted parameters for PEG-AgNPs in suspensions that include PAA at different concentrations. AgNPs grafted with relatively shorter PEG chains (molecular weight 20 kDa) show a distorted hexagonal structure in the presence of PAA with slightly smaller unit cells (see more details in Figure S3). However, for PEG5k-AgNPs, only dispersed NPs accumulate at the liquid/vapor interface in the presence of 2 mM PAA. This is based on the GISAXS line-cut intensity that decreases monotonically, with no feature that indicates diffraction, as shown in Figure 7. Figure 7b shows the line-cut intensity obtained from (a) along with a fit to a spherical form factor of ~21 nm diameter, consistent with the silver core size obtained by SAXS measurements. Although dispersed at the surface, further evidence of partial surface enrichment by PEG5K-AgNPs is obtained from the XR and extracted ED profile shown in Figure 7. Figure 7c shows R/R_F data for PEG5k-AgNPs at 0, 0.2, and 2 mM PAA. At low PAA concentrations, there is almost no evidence of film formation at the surface. At 2 mM PAA, a film is formed, but there is no in-plane ordering as indicated by the GISAXS. This again demonstrates that PAA is less effective in promoting an ordered close-packed 2D interfacial assembly of PEG-AgNPs as compared with K2CO3.

We surmise that the low grafting density of AgNPs compared with AuNPs is responsible for the inferior/distorted hexagonal structure at the liquid/vapor interface. The lower

grafting density is inferred from TGA measurements that show significant differences in the grafting density between AgNPs and AuNPs.²⁷ As examined in other polymer-grafted nanoparticle studies, the packing symmetry can be affected by the grafting density.⁴⁶ We thus propose that the lower grafting density of PEG-AgNPs induces mainly bidirectional interactions between nanoparticles forming chains upon assembly that are not transversally registered. Indeed, the weaker thiol-Ag binding interface may be dynamic and mobile, as inferred from recent studies on the nature of the thiol-Au interface, which likely promotes the rearrangement of the PEG brush on the Ag surface to favor the longitudinal alignment of PEG-AgNPs mediated by PAA. 47,48 Thus, the anisotropic arrangement proposed here is analogous to other polymer-grafted nanoparticles that assemble in various manners including chains, sheets, etc. Such directional binding has been attributed to ligand grafting mobility and density. $^{49-51}$ In contrast, the addition of K2CO3, which promotes strong PEG phase separation (by salting out), leads to close-packing interfacial assembly. 26,28 This concept is illustrated in Figure 6c,d. 52 In the SI, Figures S8 and S9 show simulations of 2D X-ray scattering interference patterns (i.e., $S(Q_{xy})$) for the amorphous assembly of dimers, trimers, and more ordered 2D lamellar structures (can also be viewed as distorted hexagonal structures) that give rise to equidistant interference peaks, indicating that there is a single dominant interparticle correlation length. Relevant parameters of the extracted structures using K₂CO₃ or PAA are listed in Table 1.

3D Crystallization. In addition to the 2D assembly at the liquid/vapor interface, we also investigate the 3D assembly of

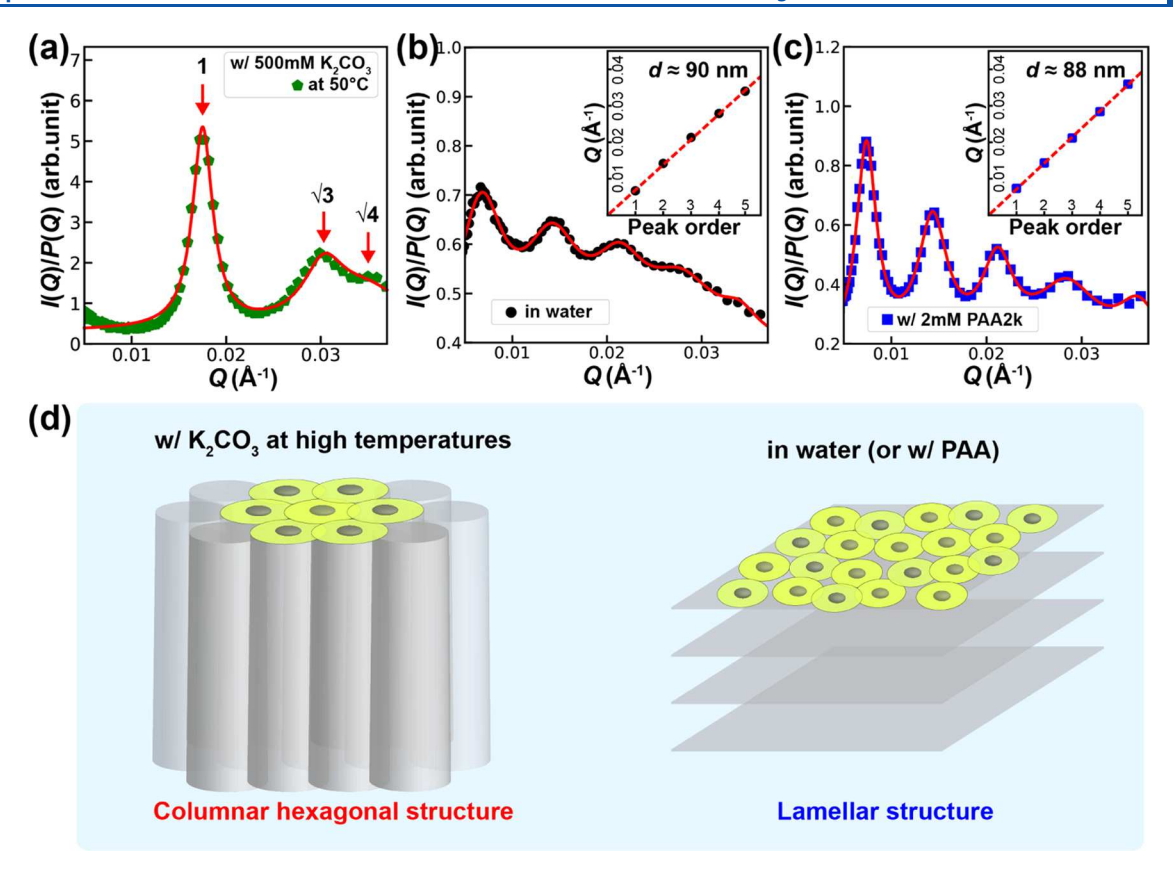


Figure 8. Extracted structure factor profiles (I(Q)/P(Q)) for PEG40k-AgNPs with (a) 500 mM K₂CO₃ at 50 °C, (b) 0 mM PAA2k, and (c) 2 mM PAA2k, respectively. The solid line represents the best-fit profile using Lorentzian-type line shapes. In (a), red arrows indicate the Q positions of higher-order Bragg diffraction peaks of a hexagonal lattice. Insets in (b) and (c): peak position, Q, as a function of the peak order with a linear fit with a slope estimation of the interparticle distance, d. (d) Schematic illustration of the self-assembly of PEG40k-AgNPs under specific solvent conditions.

Table 2. Summary of SAXS Results for PEG-AgNPs under Various Solvent Conditions

nanoparticle type	solvent condition	lattice type	$\frac{d_{hkl}}{(\text{nm})^a}$
PEG40k-AgNPs	in pure water	lamellar	90 (2)
	with 2 mM PAA2k	lamellar	88 (2)
	with 500 mM K ₂ CO ₃ ^b	columnar hexagonal	33 (1)
PEG20k-AgNPs	in pure water	lamellar	76 (3)
	with 2 mM PAA2k	lamellar	75 (1)
	with 500 mM $K_2CO_3^b$	columnar hexagonal	33 (1)
PEG5k-AgNPs	in pure water	n/a (form factor- like)	
	with 2 mM PAA2k	short-range order	59 (1)
	with 500 mM $K_2CO_3^b$	short-range order	25 (1)

^aInterparticle distance from the best-fit profile using Lorentzian-type line shapes; $d_{hkl} = 2\pi/Q_{hkl} \,^b 60 \,^{\circ}\text{C}$.

PEG-AgNPs in bulk suspensions using solution SAXS. In the presence of K_2CO_3 , the diffraction pattern, I(Q)/P(Q), shown in Figure 8a has a relative peak position ratio of $1:\sqrt{3}:\sqrt{4}$. Such a pattern suggests a columnar 3D hexagonal structure, as depicted in Figure 8d. We propose that each cylinder consists of PEG-AgNP chains that are formed by the *bidirectional* interactions mentioned above. Similar results are also obtained for PEG20k and PEG5k, as shown in Figure S7. Relevant structural parameters extracted from the SAXS data are listed in Table 2.

It is interesting to note that in pure aqueous solution, the diffraction pattern consists of peaks with a relative position ratio of 1:2:3:4:5, as shown in Figure 8b. However, a more enhanced structure factor profile is obtained in the presence of PAA, as shown in Figure 8c. Such a pattern is generally associated with a lamellar structure, as illustrated in Figure 8d. As argued above, we suggest that each layer consists of a sheet of distorted hexagonal structure as discussed above. Additional 3D SAXS data analytical results for AgNPs grafted with relatively short PEG chains are provided in the SI (Figure S6).

CONCLUSIONS

We successfully grafted silver nanoparticles with thiolated PEG of various molecular weights. Our TGA measurements indicate a low grafting density of PEG-AgNPs compared with PEG-AuNPs. Adding either K₂CO₃ or PAA in suspensions induces the assembly of the grafted PEG-AgNPs at the liquid/vapor interface and in the bulk. However, the addition of K₂CO₃ leads to the formation of a 2D hexagonal structure and the addition of PAA leads to a lamella-like structure at the liquid/ vapor interface. We argue that due to the lower grafting density for AgNPs compared with AuNPs, AgNPs tend to form chains that are not registered as ideal hexagonal structures. The addition of K₂CO₃ promotes phase separation and interfacial crystallization more efficiently (by salting out). PAA may form a hydrogen bond with PEG-AgNPs, disrupting the crystallinity.^{26,28} The bulk assembly determined by SAXS measurements shows a significant difference between the addition of $\rm K_2CO_3$ and PAA. The addition of $\rm K_2CO_3$ likely leads to a columnar 3D hexagonal structure, and the addition of PAA induces a 3D lamellar structure. We propose that due to the low grafting density, PEG-AgNPs are inclined to form bidirectional interactions that lead to the formation of chains. These chains are the building blocks for the observed 2D structures and the 3D columnar and lamellar structures. These findings show that the effect of the core type of nanoparticles can be employed to facilitate direction-mediated assembly, which can be used for assembly in applications involving plasmonics or photonics.

ASSOCIATED CONTENT

Supporting Information

The Supporting Information is available free of charge at https://pubs.acs.org/doi/10.1021/acsanm.2c03042.

Thermogravimetric analysis of PEG-AgNPs; form factor analysis for AgNPs; GISAXS, XR, and 3D SAXS data for PEG-AgNPs; simulation of the interference patterns expected for GISAXS from a lamella-like 2D assembly (PDF)

AUTHOR INFORMATION

Corresponding Authors

Surya K. Mallapragada – Ames National Laboratory, and Department of Chemical and Biological Engineering, Iowa State University, Ames, Iowa 50011, United States;

orcid.org/0000-0002-9482-7273; Email: suryakm@iastate.edu

David Vaknin — Ames National Laboratory, and Department of Physics and Astronomy, Iowa State University, Ames, Iowa 50011, United States; Orcid.org/0000-0002-0899-9248; Email: vaknin@ameslab.gov

Authors

Hyeong Jin Kim – Ames National Laboratory, and Department of Chemical and Biological Engineering, Iowa State University, Ames, Iowa 50011, United States; orcid.org/0000-0001-9180-0430

Wenjie Wang — Division of Materials Sciences and Engineering, Ames National Laboratory, U.S. DOE, Ames, Iowa 50011, United States; © orcid.org/0000-0002-7079-1691

Wei Bu − NSF's ChemMatCARS, University of Chicago, Chicago, Illinois 60637, United States; orcid.org/0000-0002-9996-3733

Complete contact information is available at: https://pubs.acs.org/10.1021/acsanm.2c03042

Notes

The authors declare no competing financial interest.

ACKNOWLEDGMENTS

This study was supported by the U.S. Department of Energy (U.S. DOE), Office of Basic Energy Sciences, Division of Materials Sciences and Engineering. The Ames National Laboratory is operated for the U.S. DOE by Iowa State University under Contract DE-AC02-07CH11358. NSF's ChemMatCARS Sector 15 is supported by the Divisions of Chemistry (CHE) and Materials Research (DMR), National Science Foundation, under grant number NSF/CHE-1834750. The use of the Advanced Photon Source, an Office of Science

User Facility operated for the U.S. Department of Energy (DOE) Office of Science by Argonne National Laboratory, was supported by the U.S. DOE under Contract No. DE-AC02-06CH11357. The authors thank the 12ID-B beamline staff for synchrotron beamline support in SAXS measurements at the Advanced Photon Source, Argonne National Laboratory.

REFERENCES

- (1) Sagiv, J. Organized monolayers by adsorption. 1. Formation and structure of oleophobic mixed monolayers on solid surfaces. *J. Am. Chem. Soc.* **1980**, *102*, 92–98.
- (2) Nuzzo, R. G.; Allara, D. L. Adsorption of bifunctional organic disulfides on gold surfaces. *J. Am. Chem. Soc.* 1983, 105, 4481–4483.
- (3) Ulman, A. Formation and structure of self-assembled monolayers. Chem. Rev. 1996, 96, 1533-1554.
- (4) Love, J. C.; Estroff, L. A.; Kriebel, J. K.; Nuzzo, R. G.; Whitesides, G. M. Self-assembled monolayers of thiolates on metals as a form of nanotechnology. *Chem. Rev.* **2005**, *105*, 1103–1170.
- (5) Neouze, M.-A.; Schubert, U. Surface modification and functionalization of metal and metal oxide nanoparticles by organic ligands. *Monatsh. Chem.* **2008**, *139*, 183–195.
- (6) Ruckenstein, E.; Li, Z. Surface modification and functionalization through the self-assembled monolayer and graft polymerization. *Adv. Colloid Interface Sci.* **2005**, *113*, 43–63.
- (7) Vericat, C.; Vela, M. E.; Corthey, G.; Pensa, E.; Cortés, E.; Fonticelli, M. H.; Ibanez, F.; Benitez, G.; Carro, P.; Salvarezza, R. C. Self-assembled monolayers of thiolates on metals: a review article on sulfur-metal chemistry and surface structures. *RSC Adv.* **2014**, *4*, 27730–27754.
- (8) Templeton, A. C.; Wuelfing, W. P.; Murray, R. W. Monolayer-protected cluster molecules. *Acc. Chem. Res.* **2000**, *33*, 27–36.
- (9) Schreiber, F. Structure and growth of self-assembling monolayers. *Prog. Surf. Sci.* **2000**, *65*, 151–257.
- (10) Mirkin, C. A.; Letsinger, R. L.; Mucic, R. C.; Storhoff, J. J. A DNA-based method for rationally assembling nanoparticles into macroscopic materials. *Nature* **1996**, 382, 607–609.
- (11) Mattoussi, H.; Mauro, J. M.; Goldman, E. R.; Anderson, G. P.; Sundar, V. C.; Mikulec, F. V.; Bawendi, M. G. Self-assembly of CdSe-ZnS quantum dot bioconjugates using an engineered recombinant protein. *J. Am. Chem. Soc.* **2000**, *122*, 12142–12150.
- (12) Feng, L.; Zhu, C.; Yuan, H.; Liu, L.; Lv, F.; Wang, S. Conjugated polymer nanoparticles: preparation, properties, functionalization and biological applications. *Chem. Soc. Rev.* **2013**, 42, 6620–6633.
- (13) Kovalenko, M. V.; Manna, L.; Cabot, A.; Hens, Z.; Talapin, D. V.; Kagan, C. R.; Klimov, V. I.; Rogach, A. L.; Reiss, P.; Milliron, D. J.; Guyot-Sionnnest, P.; Konstantatos, G.; Parak, W. J.; Hyeon, T.; Korgel, B. A.; Murray, C. B.; Heiss, W. Prospects of nanoscience with nanocrystals. ACS Nano 2015, 9, 1012–1057.
- (14) Boles, M. A.; Engel, M.; Talapin, D. V. Self-assembly of colloidal nanocrystals: From intricate structures to functional materials. *Chem. Rev.* **2016**, *116*, 11220–11289.
- (15) Macfarlane, R. J.; Lee, B.; Jones, M. R.; Harris, N.; Schatz, G. C.; Mirkin, C. A. Nanoparticle Superlattice Engineering with DNA. *Science* **2011**, 334, 204–208.
- (16) Nykypanchuk, D.; Maye, M. M.; Van Der Lelie, D.; Gang, O. DNA-guided crystallization of colloidal nanoparticles. *Nature* **2008**, 451, 549–552.
- (17) Laramy, C. R.; O'Brien, M. N.; Mirkin, C. A. Crystal engineering with DNA. Nat. Rev. Mater. 2019, 4, 201-224.
- (18) Szekrényes, D. P.; Hamon, C.; Constantin, D.; Deak, A. Formation of Kinetically Trapped Small Clusters of PEGylated Gold Nanoparticles Revealed by the Combination of Small-angle X-ray Scattering and Visible Light Spectroscopy. *Soft Matter* **2022**, *18*, 8295.
- (19) Zámbó, D.; Radnóczi, G. Z.; Deák, A. Preparation of compact nanoparticle clusters from polyethylene glycol-coated gold nanoparticles by fine-tuning colloidal interactions. *Langmuir* **2015**, *31*, 2662–2668.

- (20) Zhang, H.; Wang, W.; Akinc, M.; Mallapragada, S.; Travesset, A.; Vaknin, D. Assembling and ordering polymer-grafted nanoparticles in three dimensions. *Nanoscale* **2017**, *9*, 8710–8715.
- (21) Choueiri, R. M.; Klinkova, A.; Thérien-Aubin, H.; Rubinstein, M.; Kumacheva, E. Structural transitions in nanoparticle assemblies governed by competing nanoscale forces. *J. Am. Chem. Soc.* **2013**, *135*, 10262–10265.
- (22) Nayak, S.; Horst, N.; Zhang, H.; Wang, W.; Mallapragada, S.; Travesset, A.; Vaknin, D. Interpolymer complexation as a strategy for nanoparticle assembly and crystallization. *J. Phys. Chem. C* **2019**, *123*, 836–840
- (23) Zhang, H.; Wang, W.; Mallapragada, S.; Travesset, A.; Vaknin, D. Ion-specific interfacial crystallization of polymer-grafted nanoparticles. *J. Phys. Chem. C* **2017**, *121*, 15424–15429.
- (24) Zhang, H.; Wang, W.; Mallapragada, S.; Travesset, A.; Vaknin, D. Macroscopic and Tunable Nanoparticle Superlattices. *Nanoscale* **2017**, *9*, 164–171.
- (25) Kim, H. J.; Hossen, M. M.; Hillier, A. C.; Vaknin, D.; Mallapragada, S. K.; Wang, W. Interfacial and bulk assembly of anisotropic gold nanostructures: implications for photonics and plasmonics. *ACS Appl. Nano Mater.* **2020**, *3*, 8216–8223.
- (26) Kim, H. J.; Wang, W.; Travesset, A.; Mallapragada, S. K.; Vaknin, D. Temperature-induced tunable assembly of columnar phases of nanorods. *ACS Nano* **2020**, *14*, 6007–6012.
- (27) Kim, H. J.; Wang, W.; Zhang, H.; Freychet, G.; Ocko, B. M.; Travesset, A.; Mallapragada, S. K.; Vaknin, D. Effect of Polymer Chain Length on the Superlattice Assembly of Functionalized Gold Nanoparticles. *Langmuir* **2021**, *37*, 10143–10149.
- (28) Kim, H. J.; Wang, W.; Mallapragada, S. K.; Vaknin, D. The Effects of Temperature on the Assembly of Gold Nanoparticle by Interpolymer Complexation. *J. Phys. Chem. Lett.* **2021**, *12*, 1461–1467.
- (29) Kim, H. J.; Wang, W.; Mallapragada, S.; Travesset, A.; Vaknin, D. Nanoparticle Superlattices with Negative Thermal Expansion (NTE) Coefficients. *J. Phys. Chem. C* **2021**, *125*, 10090–10095.
- (30) Kim, H. J.; Wang, W.; Zhang, H.; Freychet, G.; Ocko, B. M.; Travesset, A.; Mallapragada, S. K.; Vaknin, D. Binary Superlattices of Gold Nanoparticles in Two Dimensions. *J. Phys. Chem. Lett.* **2022**, *13*, 3424–3430.
- (31) Minier, S.; Kim, H. J.; Zaugg, J.; Mallapragada, S. K.; Vaknin, D.; Wang, W. Poly (N-isopropylacrylamide)-grafted gold nanoparticles at the vapor/water interface. *J. Colloid Interface Sci.* **2021**, 585, 312–319.
- (32) Pakiari, A. H.; Jamshidi, Z. Nature and strength of M- S Bonds (M= Au, Ag, and Cu) in binary alloy gold clusters. *J. Phys. Chem. A* **2010**, *114*, 9212–9221.
- (33) Lee, J.-S.; Kim, H.; Algar, W. R. Thiol-ligand-Catalyzed quenching and etching in mixtures of colloidal quantum dots and silver nanoparticles. *J. Phys. Chem. C* **2017**, *121*, 28566–28575.
- (34) Gondikas, A. P.; Morris, A.; Reinsch, B. C.; Marinakos, S. M.; Lowry, G. V.; Hsu-Kim, H. Cysteine-induced modifications of zero-valent silver nanomaterials: implications for particle surface chemistry, aggregation, dissolution, and silver speciation. *Environ. Sci. Technol.* **2012**, *46*, 7037–7045.
- (35) Marchioni, M.; Gallon, T.; Worms, I.; Jouneau, P.-H.; Lebrun, C.; Veronesi, G.; Truffier-Boutry, D.; Mintz, E.; Delangle, P.; Deniaud, A.; Michaud-Soret, I. Insights into polythiol-assisted AgNP dissolution induced by bio-relevant molecules. *Environ. Sci.: Nano* 2018, 5, 1911–1920.
- (36) Marchioni, M.; Battocchio, C.; Joly, Y.; Gateau, C.; Nappini, S.; Pis, I.; Delangle, P.; Michaud-Soret, I.; Deniaud, A.; Veronesi, G. Thiolate-Capped Silver Nanoparticles: Discerning Direct Grafting from Sulfidation at the Metal—Ligand Interface by Interrogating the Sulfur Atom. *J. Phys. Chem. C* **2020**, *124*, 13467—13478.
- (37) Motellier, S.; Römer, I.; Pélissier, N.; Valsami-Jones, E. On the transformation mechanism of polyethylene glycol-and citrate-coated silver nanocolloids under sunlight exposure. *J. Nanopart. Res.* **2019**, 21, 163.

- (38) Stetefeld, J.; McKenna, S. A.; Patel, T. R. Dynamic light scattering: a practical guide and applications in biomedical sciences. *Biophys. Rev.* **2016**, *8*, 409–427.
- (39) Swinehart, D. F. The beer-lambert law. *J. Chem. Educ.* **1962**, *39*, 333.
- (40) Vaknin, D.X-Ray Diffraction and Spectroscopic Techniques for Liquid Surfaces and Interfaces *Characterization of Materials*, Kaufmann, E. N. Ed., John Wiley & Sons, Inc., 2012, DOI: 10.1002/0471266965.com077.pub2.
- (41) Als-Nielsen, J.; McMorrow, D. Elements of Modern X-ray Physics; John Wiley & Sons, 2011.
- (42) Pershan, P. S.; Schlossman, M.Liquid Surfaces and Interfaces: Synchrotron X-ray Methods, Cambridge University Press, 2012.
- (43) Li, T.; Senesi, A. J.; Lee, B. Small angle X-ray scattering for nanoparticle research. *Chem. Rev.* **2016**, *116*, 11128–11180.
- (44) Mangenot, S.; Leforestier, A.; Durand, D.; Livolant, F. X-ray diffraction characterization of the dense phases formed by nucleosome core particles. *Biophys. J.* **2003**, *84*, 2570–2584.
- (45) Zaluzhnyy, I. A.; Kurta, R. P.; Scheele, M.; Schreiber, F.; Ostrovskii, B. I.; Vartanyants, I. A. Angular x-ray cross-correlation analysis (AXCCA): Basic concepts and recent applications to soft matter and nanomaterials. *Materials* **2019**, *12*, 3464.
- (46) Yun, H.; Yu, J. W.; Lee, Y. J.; Kim, J.-S.; Park, C. H.; Nam, C.; Han, J.; Heo, T.-Y.; Choi, S.-H.; Lee, D. C.; Lee, W. B.; Stein, G. E.; Kim, B. J. Symmetry transitions of polymer-grafted nanoparticles: Grafting density effect. *Chem. Mater.* **2019**, *31*, 5264–5273.
- (47) Bürgi, T. Properties of the gold, Asialphur interface: from self-assembled monolayers to clusters. *Nanoscale* **2015**, *7*, 15553–15567.
- (48) Inkpen, M. S.; Liu, Z.; Li, H.; Campos, L. M.; Neaton, J. B.; Venkataraman, L. Non-chemisorbed gold-sulfur binding prevails in self-assembled monolayers. *Nat. Chem.* **2019**, *11*, 351–358.
- (49) Jiao, Y.; Akcora, P. Assembly of polymer-grafted magnetic nanoparticles in polymer melts. *Macromolecules* **2012**, *45*, 3463–3470.
- (50) Yockell-Lelièvre, H.; Desbiens, J.; Ritcey, A. M. Two-dimensional self-organization of polystyrene-capped gold nanoparticles. *Langmuir* **2007**, 23, 2843–2850.
- (51) Kumar, S. K.; Kumaraswamy, G.; Prasad, B. L.; Bandyopadhyaya, R.; Granick, S.; Gang, O.; Manoharan, V. N.; Frenkel, D.; Kotov, N. A. Nanoparticle assembly: a perspective and some unanswered questions. *Current Science* **2017**, *112*, 1635–1641.
- (52) Vial, S.; Nykypanchuk, D.; Yager, K. G.; Tkachenko, A. V.; Gang, O. Linear mesostructures in DNA—nanorod self-assembly. *ACS Nano* **2013**, *7*, 5437—5445.